**SERBIAN JOURNAL OF ELECTRICAL ENGINEERING**
**Vol. 8, No. 2, May 2011, 181-201**

**UDK: 004.383.3**

# FPGA-Based Control of Piezoelectric Actuators

**László Juhász[1], Jürgen Maas[1]**

**Abstract:** In many industrial applications like semiconductor production and optical inspection systems, the availability of positioning systems capable to follow trajectory paths in the range of several centimetres, featuring at the same time a nanometre-range precision, is demanding. Pure piezoelectric stages and standard positioning systems with motor and spindle are not able to meet such requirements, because of the small operation range and inadequacies like backlash and friction. One concept for overcoming these problems consists of a hybrid positioning system built through the integration of a DC-drive in series with a piezoelectric actuator. The wide range of potential applications enables a considerable market potential for such an actuator, but due to the high variety of possible positioned objects and dynamic requirements, the required control complexity may be significant.

In this paper, a real-time capable state-space control concept for the piezoelectric actuators, embedded in such a hybrid micropositioning system, is presented. The implementation of the controller together with a real-time capable hysteresis compensation measure is performed using a low-budget FPGA-board, whereas the superimposed integrated controller is realized with a dSPACE RCP-system. The advantages of the designed control over a traditional proportional-integral control structure are proven through experimental results using a commercially available hybrid micropositioning system. Positioning results by different dynamic requirements featuring positioning velocities from 1 μm/s up to 5 cm/s are given.

**Keywords:** Hybrid nanopositioning system, Piezoelectric actuator, State-space controller, Hysteresis compensation, FPGA.

## 1 Introduction

In various industrial applications, the availability of positioning systems capable to follow trajectory paths in the range of several centimetres, featuring at the same time a nanometre-range precision, is demanding [1]. The spectrum of such applications includes atomic force and white-light microscopy [2], semiconductor manufacturing, precision optics alignment, wire feeding systems [3], microbiological cell manipulation, ultra-precision machine tools and micro-

---

[1] Ostwestfalen-Lippe University of Applied Sciences, Lemgo, Liebigstrasse 87, Germany 119;
E-mail: Laszlo.Juhasz@hs-owl.de

robots, as well as the fields like strategic defence, space technologies, astronomy [4], and laser nuclear ignition target production [1]. Thereby, depending on the concrete application, the required positioning velocities vary between a few micrometers and several centimeters per second.

Pure piezoelectric stages and standard positioning systems with motor and spindle are not able to meet such requirements. On the one hand, piezoelectric actuators (PEA) have highly limited working range, usually only a few micrometers. The very small working volume is limited by the change of the actuator dimensions, since one end of the actuator is fixed to the base. Using sequentially connected actuators ("stacked design"), the working capacity can be enlarged in a limited range. On the other hand, the dynamic positioning precision of a standard motor-spindle driven mechanism is severely limited by inadequacies like friction and backlash. The correction of these structural problems using a feed-forward or feedback controller represents a difficult task, which sometimes cannot be solved in an appropriate way.

Therefore, different approaches have recently been investigated in order to allow the construction of a micropositioning system featuring high accuracy, large operation range, and highly variable positioning speed. One solution for the mentioned requirements is represented by hybrid micropositioning systems (HMS), built through a combination of two different actuators. The "conventional" actuator (for example, an AC or DC motor with gearbox, a linear drive, or a pneumatic system) is responsible for the coarse motion. A second actuator, being mainly a "non-conventional" one (for example a PEA or a voice coil) realizes the fine motion. Both actuators are mechanically coupled and make an integrated positioning system. The object position and speed by such an HMS depends on the position and velocity of both actuators.

Such a system, presented in [5], consists of cascaded mechanical coupling of a hydraulic actuator and a PEA. Chen and Dwang [6] presented an approach with a ball-screw drive mechanism featuring a piezoelectric nut for active ball-screw preload and the fine motion control. An improved nanopositioning system based on a similar approach was presented in [7]. Liu [8] and Glöß [9] proposed the cascaded mechanical coupling of a DC-drive and a PEA for the use in positioning systems with one or more degrees of freedom.

With an HMS operation ranges larger than 100 mm with positioning velocities up to 100 mm/s can be achieved, maintaining at the same time nanometer-range positioning accuracy. Through the use of high-resolution positioning sensors and adequate control algorithm, excellent positioning features like high-precision repeatability, short settling times and accurate trajectory-tracking during object motion are possible. Because of the wide spectrum of potential applications, there is on one hand a considerable market potential for such an actuator. However, the efforts needed to design a suitable control law, on the other hand, may reach significant complexity due to the high variety of possible positioned objects and positioning rules.

This paper gives first a brief description of the HMS under investigation. As next, the integrated control system is presented. The main chapter describes the design of the PEA controller. Finally, the practical implementation on a low-budget FPGA and the achieved experimental results with the integrated control system are presented.

Although the presented controller design addresses a PEA embedded in an HMS, it can be applied for other micropositioning systems using a PEA, as well.

## 2 The Hybrid Micropositioning Stage Under Investigation

The HMS under investigation is of type M-511.HD, manufactured by Physik Instrumente ([9], Fig. 1). It consists of a DC-drive *M* connected to a spindle, a gearbox, and two moving masses with a pair of identical piezoelectric actuators in between.

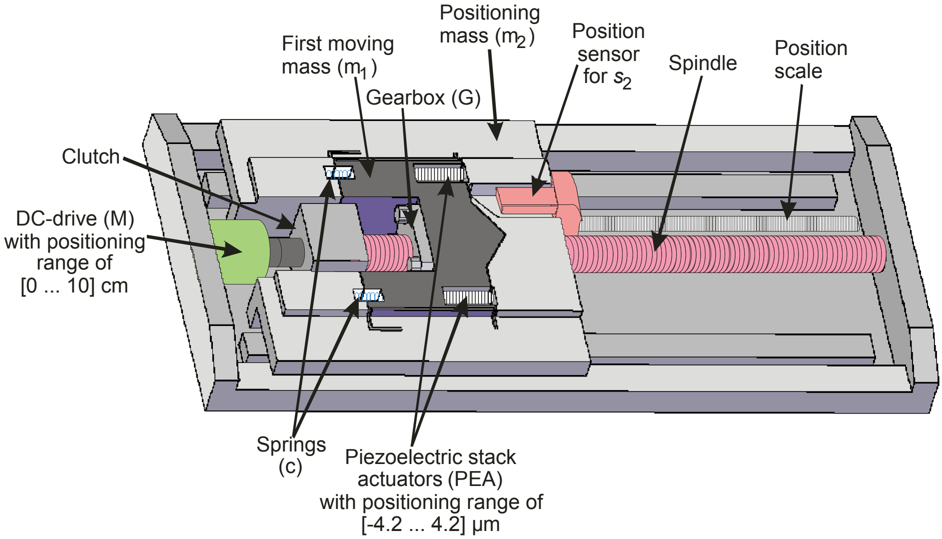

**Fig. 1** – *Drawing of the* HMS *under investigation.*

The DC drive moves the masses $m_1$ and $m_2$ together, whereas the PEA achieves an additional differential movement of $m_2$ relative to $m_1$. By controlling the voltage $v_{PWM}$, the angular position of the DC-drive $\varepsilon_M$ can be regulated. The achieved angular position $\varepsilon_M$ is converted into linear motion of the first moving mass $m_1$ by the gearbox *G* of reduction ratio $i_{rt}$. Between the masses $m_1$ and $m_2$ there is a pair of piezoelectric stack actuators (*PEA*), each of them mounted in parallel with a preload spring $c$. By exciting the piezoelectric actuators with identical voltage $v_{PA}$, it is possible to achieve an additional motion of the second mass $m_2$ relative to $s_1$ (the position of the first mass $m_1$). The object *O* (object to be positioned, not shown in Fig. 1) is fixed to the mass $m_2$. Its linear position $s_2$ is detected by a high-precision incremental sensor of 2 nm final resolution. An equivalent schematic representation of the system is given in Fig. 2. The PEA pair and the springs are represented here with a single equivalent actuator *P*, connected in parallel to a single equivalent spring $c$, whereas $J_m$ represents the equivalent inertia moment of the DC motor together with the spindle.

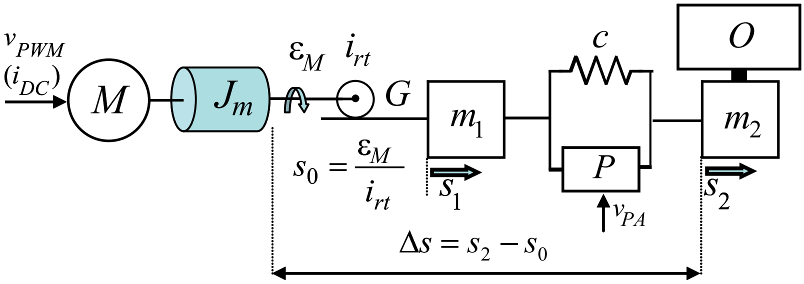

**Fig. 2** – *Schematic representation of a hybrid micropositioning system.*

A parameterized physical model of this HMS is presented in [10]. This model will be used here for the controller design with a slight modification: the rotating motion of the DC drive is represented with a transformed linear movement by the transformation ratio $i_{rt}$. Accordingly, parameters given in the rotating coordinate system are replaced with the equivalent ones for linear movement. Particularly, $\varepsilon_M$ is replaced by $s_0$ and $J_m$ by $m_0$.

## 3 The Integrated Control Structure

### 3.1 Plant and control structure

Considering its input/output behavior, the HMS represents a MISO (multiple inputs, single output) plant (Fig. 3a). The controlled variable is the position $s_2$ which can be directly measured. The dependence of $s_2$ on the DC drive current $i_{DC}$ and the PEA voltage $v_{PA}$ can be described in the frequency domain through the transfer functions $G_{s_2/i_{DC}}$ and $G_{s_2/v_{PA}}$ (1), which can be obtained from the plant state-space model [10].

$$s_2(s) = G_{s_2/i_{DC}}(s)i_{DC}(s) + G_{s_2/v_{PA}}(s)v_{PA}(s)\,. \tag{1}$$

Certain approaches to control design based on such plant description are investigated in [10]. Besides of the high order of the transfer functions $G_{s2/i_{DC}}$ and $G_{s2/v_{PA}}$, the main issue is the proper distribution of the control signal onto both actuators, regarding their individual dynamic properties and the very limited operating range of the PEA (+/– 4.2 μm).

Considering the inner states of the plant model and choosing the position $s_0$ and the position difference $\Delta s = s_2 - s_0$ as controlled variables, a MIMO (multiple inputs, multiple outputs) plant structure is obtained (Fig. 3b). This plant is described through:

$$\begin{gathered} s_0(s) = G_{s_0/i_{DC}}(s)i_{DC}(s) + G_{s_0/v_{PA}}(s)v_{PA}(s), \\ \Delta s(s) = G_{\Delta s/i_{DC}}(s)i_{DC}(s) + G_{\Delta s/v_{PA}}(s)v_{PA}(s), \\ s_2(s) = s_0(s) + \Delta s(s). \end{gathered} \tag{2}$$

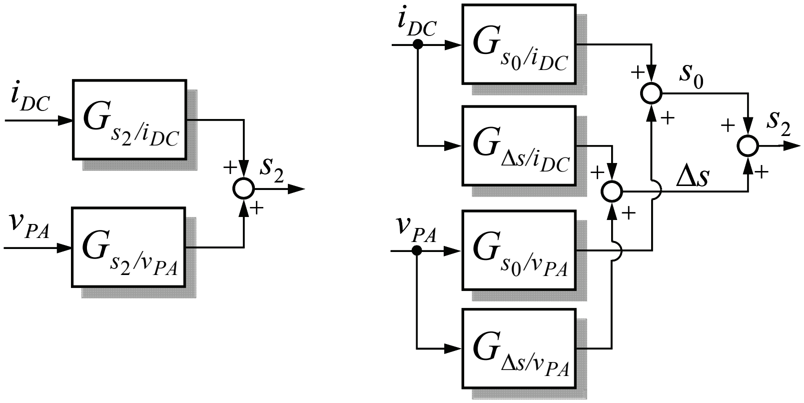

(a) (b)

**Fig. 3** – *Different plant representations.*

It can be shown that both the influence of the PEA on $s_0$, and the one of the DC drives on $\Delta s$, for the given system, is not significant and tends to zero at steady-state. Although these influences (in Fig. 3b represented by the transfer functions $G_{\Delta s/i_{DC}}$ and $G_{s_0/v_{PA}}$) can be neglected in a first approximation [11], the involvement of a decoupling network [12] improves the overall control quality. The resulting structure then consists (regarding the reference inputs and control signals) of two independent single-input-single-output (SISO) plants, modeled as:

$$\begin{aligned} s_0(s) &= \tilde{i}_{DC}(s) G_{s_0/i_{DC}}(s), \\ \Delta s(s) &= \tilde{v}_{PA}(s) G_{\Delta s/v_{PA}}(s). \end{aligned} \tag{3}$$

Hence, an independent controller design for both actuators is separately possible. The resulting control structure is displayed in Fig. 4. The selection of reference input values both for the controller of the DC-drive ($C_{DC}$) and the PEA ($C_{PEA}$) is performed according to [11].

The design of the state-space controller $C_{DC}$ for the DC-drive is described in [11], and hence it is not discussed here.

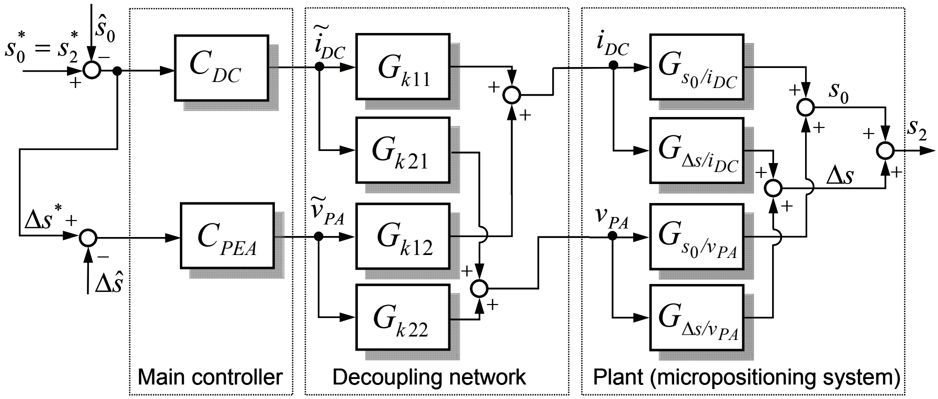

**Fig. 4** – *The integrated control structure.*

## 3.2 Estimation of plant states

The estimation of the plant inner states needed by both PEA and DC-drive controllers is performed using the linearized plant model from Fig. 5.

The linear position $s_0$ and the force $F_{DC}$ correspond to the clutch angle $\varepsilon_M$ and the DC-drive torque $T_M$.

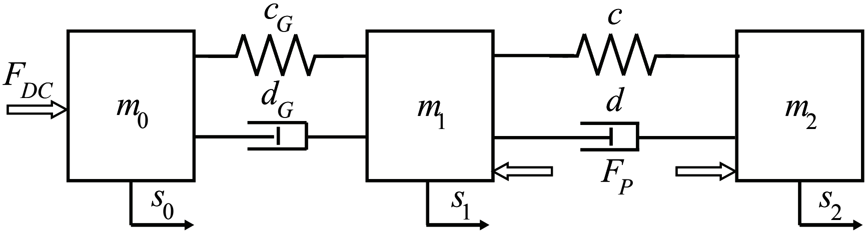

**Fig. 5** – *Simplified plant model of the micropositioning stage.*

The accurate estimation of the position differences between the masses $m_2$, $m_1$ and $m_0$ is crucial for proper controller functionality. Hence, the designed estimator is based on the position differences instead of dealing with absolute position values. Having the new state variables defined as:

$$\begin{gathered}\Delta s_1 = s_1 - s_0, \quad \Delta s_2 = s_2 - s_1, \\ \boldsymbol{x} = \begin{bmatrix}\Delta s_1 & \Delta\dot{s}_1 & \Delta s_2 & \Delta\dot{s}_2\end{bmatrix}^T, \quad \boldsymbol{u} = \begin{bmatrix}F_P & F_{DC}\end{bmatrix}^T, \quad y = \ddot{s}_2,\end{gathered} \tag{4}$$

the transformed plant model can be re-written in terms of $\Delta s_1$ and $\Delta s_2$:

$$\begin{gathered}\dot{\boldsymbol{x}} = \begin{bmatrix} 0 & 1 & 0 & 0 \\ -\left(\frac{c_G}{m_0} + \frac{c_G}{m_1}\right) & -\left(\frac{d_G}{m_0} + \frac{d_G}{m_1}\right) & \frac{c}{m_1} & \frac{d}{m_1} \\ 0 & 0 & 0 & 1 \\ \frac{c_G}{m_1} & \frac{d_G}{m_1} & -\left(\frac{c}{m_1} + \frac{c}{m_2}\right) & -\left(\frac{d}{m_1} + \frac{d}{m_2}\right) \end{bmatrix} \cdot \boldsymbol{x} + \\ + \begin{bmatrix} 0 & 0 \\ -\frac{1}{m_1} & -\frac{1}{m_0} \\ 0 & 0 \\ \frac{m_1 + m_2}{m_1 \cdot m_2} & 0 \end{bmatrix} \cdot \boldsymbol{u}, \\ \boldsymbol{y} = \begin{bmatrix} 0 & 0 & -\frac{c}{m_2} & -\frac{d}{m_2} \end{bmatrix} \cdot \boldsymbol{x} + \begin{bmatrix} \frac{1}{m_2} & 0 \end{bmatrix} \cdot \boldsymbol{u}.\end{gathered} \tag{5}$$

Using the physical plant parameter, the vector of its eigenvalues, $\boldsymbol{\lambda}$, can be calculated:

$$\boldsymbol{\lambda} = \begin{bmatrix}\lambda_1 \\ \lambda_2 \\ \lambda_3 \\ \lambda_4\end{bmatrix} = \begin{bmatrix} 381.37 \cdot \mathrm{e}^{\mathrm{j}1.614} \\ 381.37 \cdot \mathrm{e}^{-\mathrm{j}1.614} \\ -659.697 \\ -36.561 \cdot 10^3 \end{bmatrix} \cdot 2\pi \text{ [rad/s]}. \tag{6}$$

The piezoelectric amplifier can be approximated with a transfer function in the form of a first-order lag:

$$G_{PA}(s) = \frac{1}{T_{PA}s + 1}. \tag{7}$$

The time constant $T_{PA} = 80.5\ \mu\text{s}$ is estimated by its frequency response. The PEA is considered as a linear element with an electro-mechanical transform ratio $T_{EM}$ in the whole operating range because of the implemented MRC-based hysteresis compensation measure (see Section 4.1). Hence, the force $F_P$ can be calculated according to (8), whereas the calculation of $F_{DC}$ is based on the measured DC-current $i_{DC}$, the machine constant $k_m$ and the mechanical transformation ratio $i_{rt}$ (9).

$$F_P(s) = G_{PA}(s)T_{EM}V_p(s) = \frac{T_{EM}}{T_{PA}s+1}V_p(s)\,, \tag{8}$$

$$F_{DC} = i_{rt}T_M = i_{rt}k_m i_{DC}\,. \tag{9}$$

The state estimator is to be implemented on an FPGA with a sampling frequency of 100 kHz. The estimator model is thus discretized with $T_s = 10\ \mu\text{s}$ by zero-order-hold (ZOH) method [13], using the Padé-approximation [14] for the calculation of the matrix exponential.

### 3.3 The decoupling network

The dynamic decoupling network is designed using the plant transfer functions for the fulfilment of (3):

$$\boldsymbol{G}_k(s) = \begin{bmatrix} G_{k11}(s) & G_{k12}(s) \\ G_{k21}(s) & G_{k22}(s) \end{bmatrix} = \frac{1}{N_k(s)} \begin{bmatrix} G_{s0/i_{DC}}G_{\Delta s/v_{PA}} & -G_{s_0/v_{PA}}G_{\Delta s/v_{PA}} \\ -G_{s0/i_{DC}}G_{\Delta s/i_{DC}} & G_{s0/i_{DC}}G_{\Delta s/v_{PA}} \end{bmatrix}, \tag{10}$$

where $N_k(s) = G_{s0/i_{DC}}G_{\Delta s/v_{PA}} - G_{s_0/v_{PA}}G_{\Delta s/i_{DC}}$.

The calculated frequency transfer functions (10) are of 7th order and contain numerically non-realizable elements (for example a zero in the coordinate origin). Hence, these functions are approximated in the frequency range of interest with the numerically realizable functions of a lower order by reduction of neighboring pole/zero pairs, removal of the poles and zeros outside of the frequency range of interest, and involving of a low-frequency real zero $\omega_{12}$ superseding the original one:

$$\begin{gathered} G_{k11App}(s) \approx G_{k22App}(s) \approx 1, \\ G_{k12App}(s) = k_{12}\frac{(a_{12}^2+b_{12}^2)(-p_{12})}{\omega_{12}^2}\cdot \\ \cdot\frac{s^2-2\omega_{12}s+\omega_{12}^2}{s^3-(2a_{12}+p_{12})s^2+(2p_{12}+a_{12}^2+b_{12}^2)s-p_{12}(a_{12}^2+b_{12}^2)}, \\ G_{k21App}(s) = -k_{21}\frac{a_{21}^2+b_{21}^2}{z_{21}}\cdot\frac{s-z_{21}}{s^2-2a_{21}s+a_{21}^2+b_{21}^2}, \end{gathered} \tag{11}$$

where:

$$k_{12} = \lim_{t\to\infty} G_{k12}(t) = \lim_{s\to 0} G_{k12}(s) = 1,$$

$$k_{21} = \lim_{t\to\infty} G_{k21}(t) = \lim_{s\to 0} G_{k21}(s) = \frac{k_m i_{rt}[cm_1 + (c + c_G)m_2]}{c_G(m_0 + m_1 + m_2)}.$$

In (11), $a_{ij}$ and $b_{ij}$ ($i, j = 1, 2$) describes the real and imaginary part of the remaining conjugated-complex poles respectively, whereas $p_{ij}$ and $z_{ij}$ are for the remaining real poles and zeros. The gain coefficients $k_{ij}$ are obtained by fitting of the original decoupling functions. The comparisons of $G_{k12}(s)$ with $G_{k12App}(s)$ and $G_{k21}(s)$ with $G_{k21App}(s)$ are displayed in Fig. 6. The approximation errors of $G_{k11}(s)$ and $G_{k22}(s)$ are less than 0.5 dB in magnitude and 5° in phase.

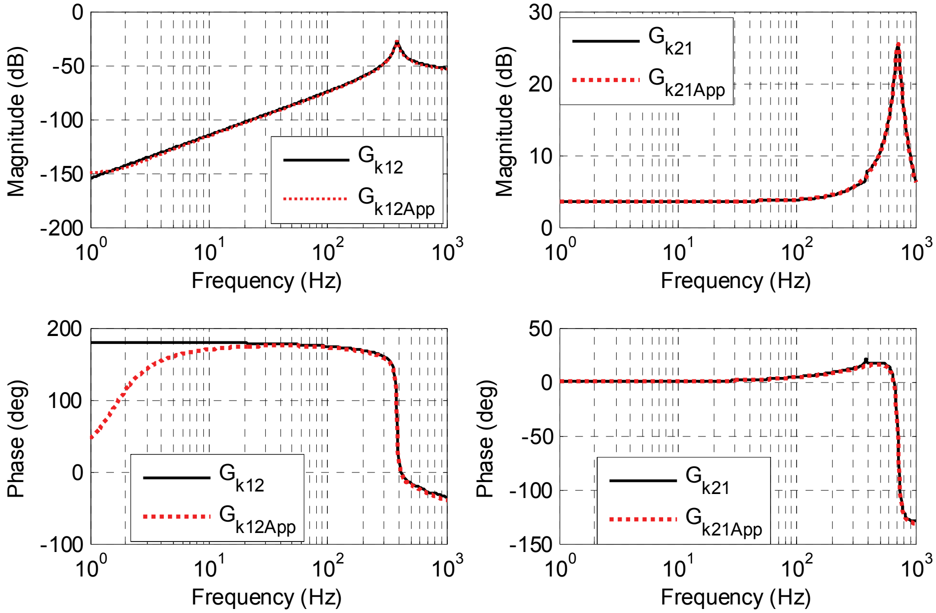

**Fig. 6** – *Approximation of* $G_{k12}$ *and* $G_{k21}$ .

The decoupling network is discretized by the Euler method and implemented on the RCP-system with a sampling frequency of 10 kHz.

# 4 Controller Design for the Piezoelectric Actuator

The PEA-controller consists of two separate modules: the feed-forward hysteresis compensation measure and the feedback state-space controller (SSC). Both modules are implemented into an FPGA, and executed in a synchronized way with 10 μs sampling time in a common process with the state estimator as displayed in Fig. 7.

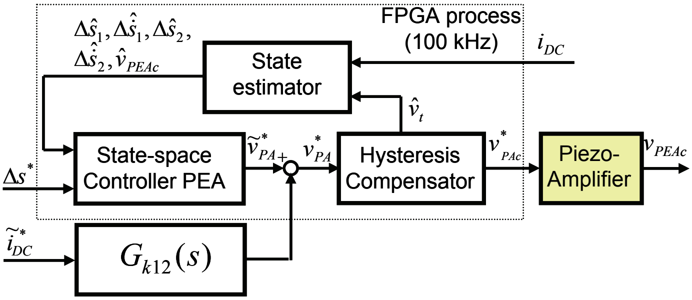

**Fig. 7** – *PEA controller consisting of the feed-forward hysteresis compensator, the state estimator, and the state-space controller.*

## 4.1 The hysteresis compensation measure

For the model-based hysteresis compensation, the Maxwell Resistive Capacitance (MRC) PEA model is chosen [15]. This model uses physical principles and includes the electric and the mechanical domain, as well as the interaction between these two domains. The integration of the chosen PEA model into the electro-mechanical model of the HMS is shown in Fig. 8. Because the mass of the PEA, $m_p$, is much smaller than $m_1$ and $m_2$, its influence is neglected. The element marked with “MRC” represents the non-linear part of the PEA-model describing the hysteresis loop. Its voltage drop depends on the current and past values of the actuator’s total charge (12). The connection between the mechanical and the electrical domain is realized through the electromechanical transformer ratio $T_{EM}$:

$$\begin{gathered} v_{mrc} = N\left(q(t),\ldots,q(t-\tau)\right), \\ v_t = v_p - v_{mrc}, \\ q = Cv_t + T_{EM}\Delta s_2. \end{gathered} \tag{12}$$

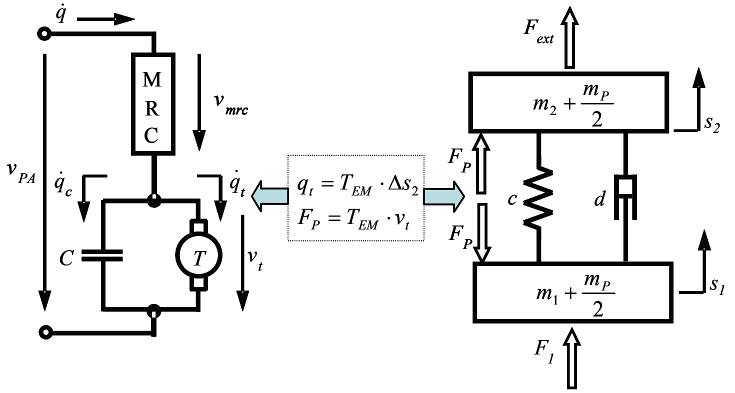

$MRC$ – Maxwell resistive capacitance
$C$ – Electrical capacity of the piezoactuator
$T_{EM}$ – Electro-mechanical transformer ratio
$F_{ext}$ – External mechanical force
$v_{PA}$ – Applied voltage to the piezoactuator
$v_{mrc}$ – Voltage of the MRC -element

$q$ – Total charge of the piezoactuator
$q_c$ – Piezoelectric capacitance charge
$q_t$ – Electro-mechanical transformer charge
$m_p$ – Effective mass of the piezoactuator
$F_1$ – Force acting on $m_1$
$v_t$ – Counter electromotive force (induced by the mechanical part)

**Fig. 8** – *The implementation of* MRC-*based* PEA *model into the model of the* HMS *under investigation.*

The dependence of the hysteresis voltage drop $v_{mrc}$ on the total charge $q$ can be modeled in different ways. In this paper, the generalized rate-independent Maxwell slip (MRC) model is used [15]. The estimation of the MRC-parameter is performed without disassembly of the HMS [16].

The hysteresis compensation measure is implemented using an additive local-feedback compensation method (ALFC, [16]). This method uses the feasibility of the chosen PEA-model to express its rate-independent part separately, in the form of a sum of a non-linear element and a unity gain (12). We present the ALFC method briefly for a more general case which is shown in Fig. 9. The plant input here is denoted with $r(t)$, its output with $y(t)$, whereas $p(t)$ is a non-measurable plant state, and $u(t)$ represents the compensator input.

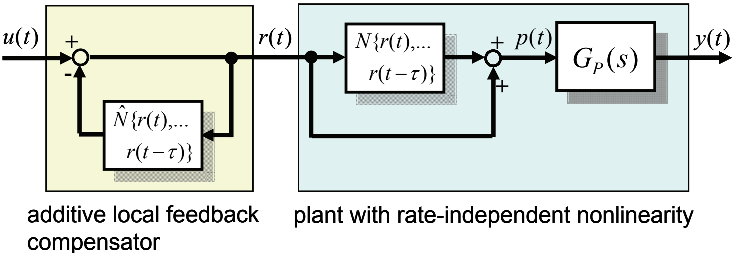

**Fig. 9** – *The* ALFC-*based nonlinearity compensation method.*

Assuming that an accurate model $\hat{N}$ for the rate-independent nonlinearity $N$ is available, the proposed compensation yields to:

$$\begin{aligned} r(t) &= u(t) - \hat{N}\{r(t),...,r(t-\tau)\}, \\ p(t) &= r(t) + N\{r(t),...,r(t-\tau)\} = \\ &= u(t) - \hat{N}\{r(t),...,r(t-\tau)\} + N\{r(t),...,r(t-\tau)\}. \end{aligned} \tag{13}$$

$$\begin{gathered} \Rightarrow p(t) \approx u(t), \quad \text{with } \hat{N} \approx N, \\ \text{respectively:} \quad Y(s) \approx G_P(s)U(s). \end{gathered} \tag{14}$$

In general, the practical implementation of such a compensator on a computer requires the solution of a fixed-point problem with memory. However, if the nonlinearity model $\hat{N}\{r(t),...,r(t-\tau)\}$ fulfils the conditions:

$$\frac{\partial \hat{N}\{r(t),...,r(t-\tau)\}}{\partial r(t)} \in R \ \wedge \ \left| \frac{\partial \hat{N}\{r(t),...,r(t-\tau)\}}{\partial r(t)} \right| < 1, \quad \forall \{r(t),...,r(t-\tau)\}\,. \tag{15}$$

then there exists an "attractive fixed point" [17] for any input signal $r$. In this case, the fixed-point problem can be discretized and replaced by a much more simple explicit difference equation:

$$r(k) = u(k) - \hat{N}\{r(k-1),...,r(k-n-1)\}\,. \tag{16}$$

Starting from the correct initial values, the compensator works correctly if the sampling frequency is significantly higher than the maximal frequency of the compensator input. The hysteresis compensator measure for the PEA is designed according to Fig. 9. The action diagram of the realized hysteresis compensator is displayed in Fig 10.

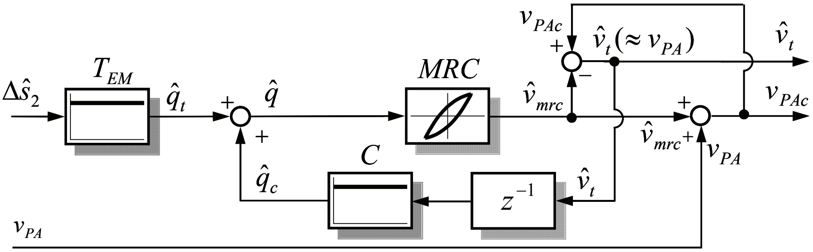

**Fig. 10** – *Action diagram of the* PEA *hysteresis compensator.*

## 4.2 The state-space controller for piezoelectric actuators

The design of the PEA state-space controller is performed using the transformed and simplified plant model from Fig. 5. Because the eigenvalue $\lambda_4$ of 36.56 kHz is outside of the frequency range of interest, it is removed from the model. This is performed by a model reduction approach, using the modal form [18]. As first, the transformation into the modal form is done according to (17) and (18). The transformation matrix $\boldsymbol{V}$ is composed of the eigenvectors $\boldsymbol{v}_i$ ($i=1,\ldots,n$) of the system matrix $\boldsymbol{A}$ obtained by solving (17).

$$(\boldsymbol{A}-\lambda_i\boldsymbol{I})\boldsymbol{v}_i=0;\quad i=1,2,...,n\,, \tag{17}$$

$$\begin{gathered}
\boldsymbol{V}=\begin{bmatrix}\boldsymbol{v}_1 & \boldsymbol{v}_2 & \ldots & \boldsymbol{v}_n\end{bmatrix}, \\
\boldsymbol{x}=\boldsymbol{V}\cdot\boldsymbol{z}=\begin{bmatrix}\boldsymbol{V}_{11} & \boldsymbol{V}_{12}\\ \boldsymbol{V}_{21} & \boldsymbol{V}_{22}\end{bmatrix}\cdot\begin{bmatrix}\boldsymbol{z}_1\\ \boldsymbol{z}_2\end{bmatrix}, \\
\dot{\boldsymbol{z}}=\boldsymbol{\Lambda}\cdot\boldsymbol{z}+\hat{\boldsymbol{B}}\cdot\boldsymbol{u},\quad \boldsymbol{y}=\hat{\boldsymbol{C}}\cdot\boldsymbol{z}+\boldsymbol{D}\cdot\boldsymbol{u}, \qquad (18) \\
\boldsymbol{\Lambda}=\boldsymbol{V}^{-1}\cdot\boldsymbol{A}\cdot\boldsymbol{V}=\begin{bmatrix}\lambda_1 & & 0\\ & ... & \\ 0 & & \lambda_4\end{bmatrix},\quad \hat{\boldsymbol{B}}=\boldsymbol{V}^{-1}\cdot\boldsymbol{B},\quad \hat{\boldsymbol{C}}=\boldsymbol{C}\cdot\boldsymbol{V}.
\end{gathered}$$

The transformed system is thereafter separated into the dominant and non-dominant subsystems (19) using the modal coordinates denoted with $\boldsymbol{z}_1$ and $\boldsymbol{z}_2$.

$$\left[\begin{array}{c}\boldsymbol{z}_1\\ \hline \boldsymbol{z}_2\end{array}\right]^{\bullet}=\left[\begin{array}{c}z_1\\ z_2\\ z_3\\ \hline z_4\end{array}\right]^{\bullet}=\left[\begin{array}{ccc:c}\lambda_1 & 0 & 0 & 0\\ 0 & \lambda_2 & 0 & 0\\ 0 & 0 & \lambda_3 & 0\\ \hdashline 0 & 0 & 0 & \lambda_4\end{array}\right]\cdot\left[\begin{array}{c}z_1\\ z_2\\ z_3\\ \hline z_4\end{array}\right]+\left[\begin{array}{c}\hat{\boldsymbol{B}}_1\\ \hdashline \hat{\boldsymbol{B}}_2\end{array}\right]\cdot\boldsymbol{u}, \tag{19}$$

$$\dot{\boldsymbol{z}}_1=\boldsymbol{\Lambda}_1\cdot\boldsymbol{z}_1+\hat{\boldsymbol{B}}_1\cdot\boldsymbol{u},\quad \dot{\boldsymbol{z}}_2=\boldsymbol{\Lambda}_2\cdot\boldsymbol{z}_2+\hat{\boldsymbol{B}}_2\cdot\boldsymbol{u}.$$

The reduced model description in the original coordinate system can thereafter be calculated using the dominant subsystem in a modal form [19]:

$$\begin{gathered}
\dot{\boldsymbol{x}}_r=\boldsymbol{F}\cdot\boldsymbol{\Lambda}_1\cdot\boldsymbol{F}^{-1}\cdot\boldsymbol{x}_r+\boldsymbol{F}\cdot\hat{\boldsymbol{B}}_1\cdot\boldsymbol{u},\\
y=\hat{\boldsymbol{C}}_1\cdot\boldsymbol{F}^{-1}\cdot\boldsymbol{x}_r+\boldsymbol{D}\cdot\boldsymbol{u},
\end{gathered} \tag{20}$$

where

$$\begin{gathered}
\boldsymbol{F}=\boldsymbol{V}_{11}+\boldsymbol{E}\cdot\boldsymbol{V}_{12}\,,\\
\boldsymbol{E}=\boldsymbol{\Lambda}_2^{-1}\cdot[\boldsymbol{B}_{21}+(\hat{\boldsymbol{B}}_2-\boldsymbol{B}_{21}\cdot\boldsymbol{B}_{11}^{-1}\cdot\hat{\boldsymbol{B}}_1)\cdot(\hat{\boldsymbol{B}}_1^{*}\cdot\boldsymbol{B}_{11}^{-1}\cdot\hat{\boldsymbol{B}}_1)^{-1}\cdot\boldsymbol{B}_1^{*}]\cdot\boldsymbol{B}_{11}^{-1}\cdot\boldsymbol{\Lambda}_1\,,\\
(\boldsymbol{B}_{11})_{i,j}=-\frac{(\hat{\boldsymbol{B}}_1\cdot\boldsymbol{Q}_u^2\cdot\hat{\boldsymbol{B}}_1^{*})_{i,j}}{\lambda_i+\overline{\lambda}_j},\quad i=1,2,3;\quad j=1,2,3\,,\\
(\boldsymbol{B}_{21})_{i,j}=-\frac{(\hat{\boldsymbol{B}}_2\cdot\boldsymbol{Q}_u^2\cdot\hat{\boldsymbol{B}}_1^{*})_{i,j}}{\lambda_{m+i}+\overline{\lambda}_j},\quad i=1;\quad j=1,2,3\,,\\
\hat{\boldsymbol{B}}_i^{*}=\mathrm{conj}(\boldsymbol{B}_i^{T}),\quad \overline{\lambda}_j=\mathrm{conj}(\lambda_j)\,.
\end{gathered}$$

Through the order reduction, the fourth state ($\Delta\dot{s}_2$) from the original state-space model is no more present in the reduced form. The reduced plant model is discretized with $T_s = 10\ \mu\text{s}$ µs by ZOH method using Padé approximation (21):

$$\begin{aligned} \boldsymbol{x}_r(k+1) &= \boldsymbol{\Phi} \cdot \boldsymbol{x}_r(k) + \boldsymbol{H} \cdot \boldsymbol{u}(k), \\ \boldsymbol{y}(k) &= \boldsymbol{C} \cdot \boldsymbol{x}(k) + \boldsymbol{D} \cdot \boldsymbol{u}(k). \end{aligned} \tag{21}$$

Equation (21) is extended with the discretized model of the piezo-amplifier (7). The resulting model is used for the design of the PEA state-space controller. After transformation in the controller canonical form [20], the transformation matrix $\boldsymbol{T}_{CP}$, the control vector $\boldsymbol{T}_{zP}$ and the input filter $q_{1P}$ are calculated using Ackermann's formula and eigenvalue assignment [20]. Pole setting for Butterworth behaviour [21] with $\omega_{gCP} = 375 \cdot 2\pi$ rad/s is chosen. The block-diagram of the realized state-space controller is shown in Fig. 11.

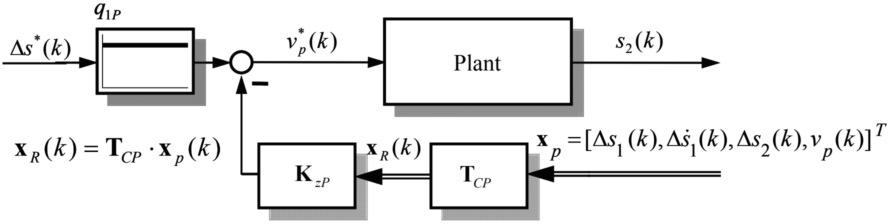

**Fig. 11** – *Block diagram of the* PEA *state-space controller.*

## 5 Practical Realization and Experimental Results

### 5.1 Practical realization of the integrated control system

Although modern central-processing-unit (CPU) based systems are powerful for complex calculations, the use of pure CPU-based systems may be inadequate by specific real-time requirements such as a highly precise timing or a high-frequency task. A suitable integration of a CPU-based system with an FPGA-board promises the solution of the mentioned problems.

The concept of the integration of a generic CPU with an FPGA through the use of a fast dual-port-memory (DPMEM) for data exchange is schematically shown in Fig. 12. The CPU ("1") is responsible for the calculation of complex algorithms and superimposed controller functionalities. The FPGA ("3") executes the underlying control functionalities dedicated to high sampling frequencies, issues control signals to the plant ("4"), reads in the sensor data, and performs all necessary pre-processing (like the calculation of the mean value of an oversampled input) on the measurement data. The data exchange between the CPU and the FPGA is solved through the DPMEM ("2").

The advantages of this concept are:

- the FPGA controls the plant directly, and very precise plant control timing is enabled,
- the CPU resources are used more efficiently, since extremely fast hardware and software interrupts are avoided – these tasks can be dedicated to the FPGA.

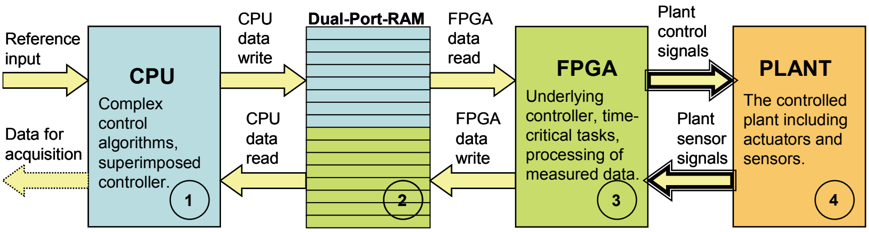

**Fig. 12** – *Integration of a* CPU *with an* FPGA *using a dual-port-random-access memory for control purposes.*

To enable these advantages, an FPGA-based interface (named as “M-CTRL interface”), featuring a Xilinx Spartan 3 FPGA is developed [22]. A rapid control prototyping (RCP) board from dSPACE is used for the superimposed control functionalities.

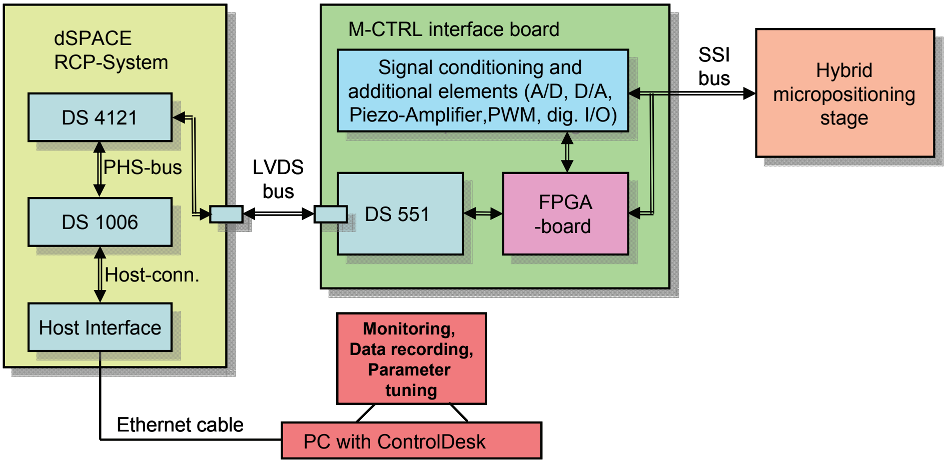

**Fig. 13** – *Overview of the experimental setup.*

The experimental system (Fig. 13) consists of the RCP system, the M-CTRL interface, and the hybrid micropositioning system M-511.HD. The data exchange between the RCP-system and the FPGA is realized with the aid of a

DS551 DPMEM-board. The PEA-controller and the state estimator are implemented in the FPGA, whereas the DC-controller and the decoupling network are realized with the RCP system. The FPGA-code is built in a modular manner: basic functionalities are written in VHDL, whereas the code of the PEA controller, hysteresis compensator and the state estimator are generated by Xilinx System Generator™. For the RCP-system, a Simulink™ blockset is written to enable appropriate DPMEM access [22].

### 5.2 Experimental results

A number of various experiments are performed to test and validate the realized control system.

Fig. 14 shows the measured static characteristic of the PEA by enabled and disabled hysteresis compensation measure. The DC-drive and the PEA feedback controller were disabled during this measurement. The characteristic by disabled hysteresis compensation measure shows a significant nonlinearity, which is almost completely eliminated when it is enabled.

Fig. 15 compares the measured responses for the position $s_2$ of the controlled PEA with the position reference ($\Delta s^*$) in the frequency domain. The DC-drive was disabled during this measurement. The response achieved by the use of a traditional proportional-integral (PI) feedback controller, designed with $40°$ phase margin, together with the response achieved with the state-space controller, are displayed. The advantages of the state controller regarding the bandwidth and resonance peaks are obvious.

Accurate tracking of a periodic position reference is required in many industrial applications. Experimental results achieved with the integrated control system by tracking of a trajectory signal of 200 μm amplitude and 1s period are shown in Fig. 16. The results are related to the case with disabled PEA controller, by enabled PEA controller but disabled decoupling network, and by enabled both PEA controller and decoupling network. The advantage of the PEA-controller and the decoupling network can be clearly noticed: the maximal dynamic tracking error and the RMSE are significantly reduced (to 202 nm and 56 nm respectively).

As can be seen, the maximal tracking error and the RMSE increased with increasing speed. However, the integrated control system works well in a velocity range from 1 μm/s up to 5 cm/s.

Tracking of large trajectories with minimal deviation by different motion speeds is frequently required in positioning tasks. Fig. 17 shows the trajectory-tracking result achieved with the integrated control system at a motion velocity of 5 mm/s over the 1 cm distance. The maximal positioning error is here 402 nm, whereas the RMSE is 98 nm. Further results for the different motion speeds and trajectory lengths are given in **Table 1**.

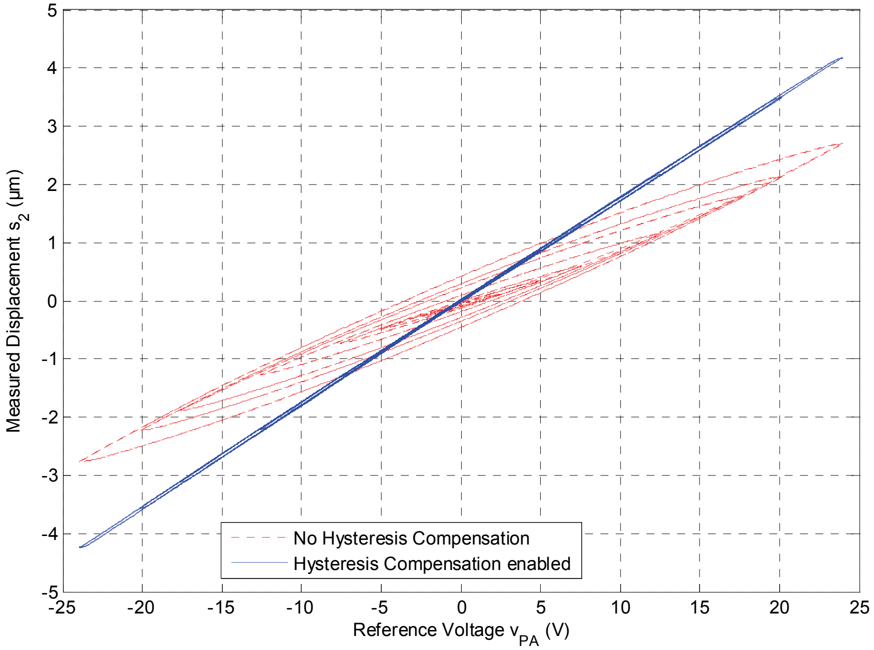

**Fig. 14** – *Input-output characteristics of the* PEA *by enabled and disabled hysteresis compensation measure.*

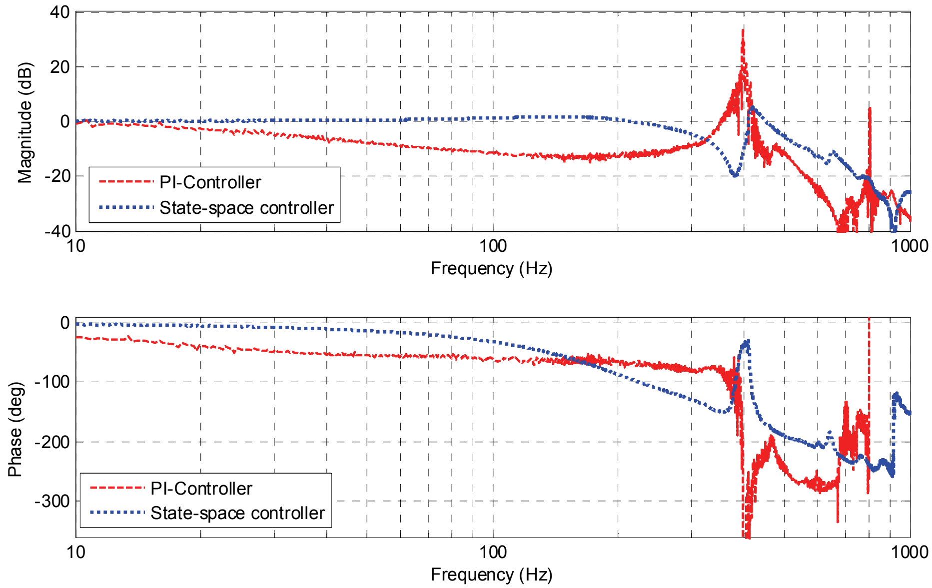

**Fig. 15** – *Measured frequency response of the controlled* PEA.

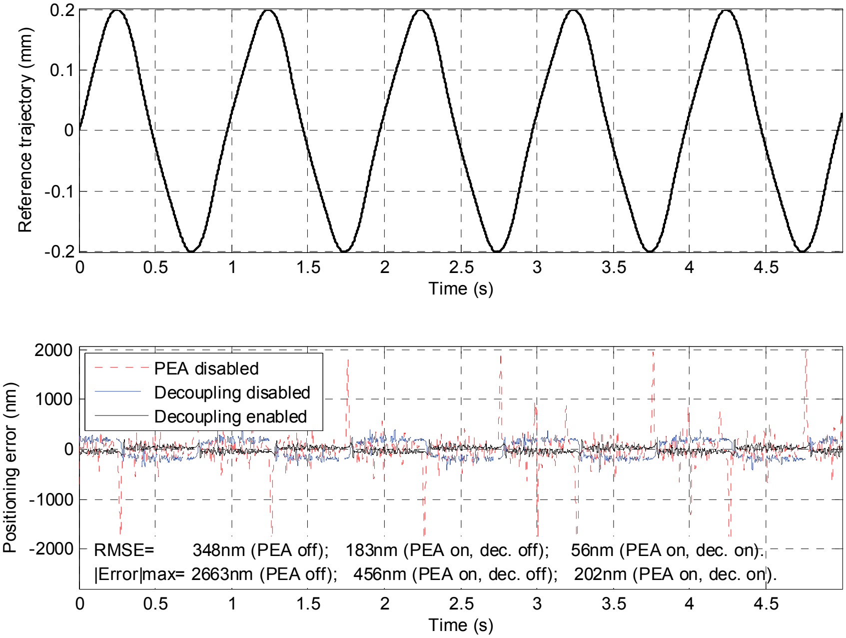

**Fig. 16** – *Tracking of a periodical trajectory signal.*

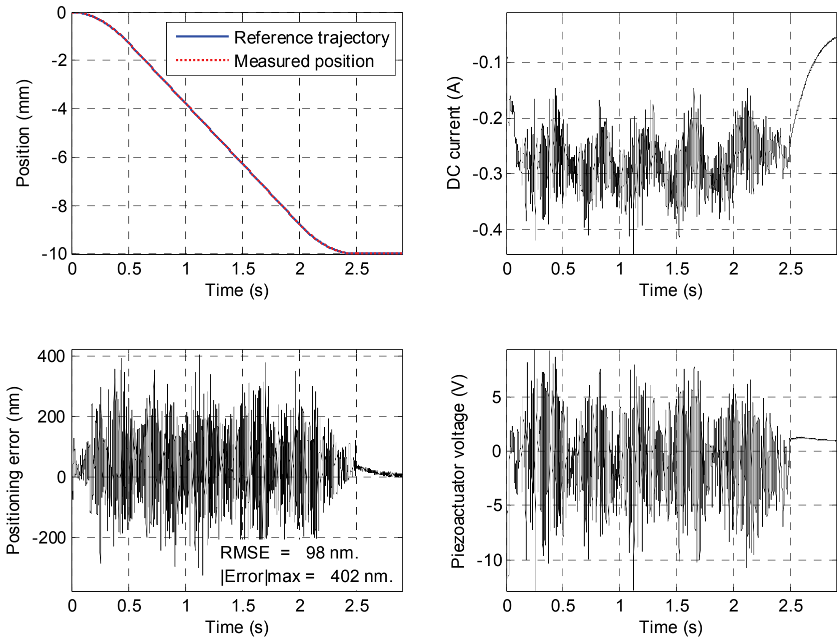

**Fig. 17** – *Experimental results by tracking a large trajectory.*

**Table 1**

*Trajectory-tracking results by different positioning velocities.*

| Maximal velocity (mm/s) | Trajectory length (mm) | Maximal dynamic tracking error (nm) | Root-mean-squared error (nm) |
|---|---|---|---|
| 50 | 20 | 1135 | 209.82 |
| 20 | 10 | 693 | 111.29 |
| 10 | 10 | 628 | 119.69 |
| 5 | 10 | 402 | 97.65 |
| 1 | 1 | 126 | 41.93 |
| 0.1 | 1 | 62 | 29.23 |
| 0.03 | 0.5 | 60 | 42.44 |
| 0.005 | 0.1 | 48 | 26.95 |
| 0.001 | 0.04 | 48 | 33.75 |

## 5 Conclusion

This paper presented an FPGA-based state-space control approach for piezoelectric actuators embedded in hybrid micropositioning systems.

The presented control design utilizes the plant representation in MIMO-form, choosing plant states for outputs instead of the measurable object position. This enables a simplification resulting in two virtually independent plants, both of them described in a SISO-form, and a decoupling network. After this simplification, a separate design of the controller for the DC-drive and the PEA is performed. To minimize trajectory-tracking errors, a state-space control concept with highly dynamic response is chosen. Estimation of the plant's internal states is done by a digital estimator model.

The PEA controller consists of the hysteresis compensation measure and a state controller. The state estimator, the hysteresis compensator, and the state-space controller of the PEA are implemented on a low-budget FPGA. The sampling frequency of both these modules is set to 100 kHz.

Experimental results show significant advantages of the presented control concepts through reduced trajectory-following error and more robust performance compared to a traditional proportional-integral feedback system.

Currently, the examination of available adaptive algorithms for online optimization of the PEA controller and the state estimator is being in progress. Such an optimization can be useful in the cases of changing environmental conditions or the positioned object.

## 6 Acknowledgements

This contribution is accomplished within the project "Adaptive Piezo-Hybridsysteme" (Adaptive Hybrid Actuated Positioning Systems), funded by the Federal Ministry of Education and Research (BMBF) of Germany under grant number 17N2108. The authors would like to thank the company Physik Instrumente for the M-511.HD device as well as Xilinx Inc. for the granted ISE software licences.

## 7 References

[1] K. Spanner, R. Glöß: New Challenges in Nanopositioning Technologies, International Conference and Exhibition on New Actuators and Drive Systems, Bremen, Germany, June, 2010, pp. 258 – 263.

[2] E. Manske, T. Hausotte, R. Mastylo, T. Machleidt, K.H. Franke, G. Jäger: New Applications of the Nanopositioning and Nanomeasuring Machine by using Advanced Tactile and Non-tactile Probes, Measurement Science and Technology, Vol. 18, No. 2, Feb. 2007, pp. 520 – 527.

[3] A. Henke, M.A. Kümmel, J. Wallaschek: A Piezoelectrically Driven Wire Feeding System for High Performance Wedge-wedge-bonding Machines, Mechatronics, Vol. 9, No. 7, Oct. 1999, pp. 757 – 767.

[4] R. Glöß, C. Enkrich, W. Schobel: Ultra-high Precision Actuator for the Primary Mirror of the 42m E-ELT Telescope, International Conference and Exhibition on New Actuators and Drive Systems, Bremen, Germany, June, 2010, pp. 1071 – 1074.

[5] M.H. Chiang, L.W. Lee, K.S. Huang: Development of a Hydraulic-piezoelectric-actuator for Hybrid Positioning Control with Large Stroke, High-loading and Sub-micrometer Accuracy, IEEE International Conference on Mechatronics, Taipei, Taiwan, July 2005, pp. 45 – 49.

[6] J.S. Chen, I.C. Dwang,: A Ballscrew Drive Mechanism with Piezo-electric Nut for Preload and Motion Control, International Journal of Machine Tools and Manufacture, Vol. 40, No. 4, March 2000, pp. 513 – 526.

[7] T. Fujita, A. Matsubara, D. Kono, I. Yamaji: Dynamic Characteristics and Dual Control of a Ball Screw Drive with Integrated Piezoelectric Actuator, Precision Engineering, Vol. 34 No.1, Jan. 2010, pp. 34 – 42.

[8] H. Liu, B. Lu, Y. Ding, Y. Tang, D. Li: A Motor-piezo Actuator for Nano-scale Positioning based on Dual Servo Loop and Nonlinearity Compensation, Journal of Micromechanics and Microengineering, Vol. 13, No. 2, March 2003, pp. 295 – 299.

[9] R. Glöß: Nanometer Precise Hybrid Actuator in Positioning Mechanism with Long Travel Range, International Conference and Exhibition on New Actuators and Drive Systems, Bremen, Germany, June 2006, pp. 668 – 671.

[10] L. Juhász, A. Kiffe, J. Maas: Modeling and Control of a Hybrid Nanopositioning, International Forum of Mechatronics, Linz, Austria, Nov. 2009, pp. 161 – 174.

[11] L. Juhász, T. Fichtner, A. Kiffe, J. Maas: Model-based State-space Control of Hybrid Micropositioning Systems, 5th IFAC Symposium on Mechatronic Systems, Cambridge, MA, USA, Sept. 2010, pp. 324 – 331.

[12] Q.G. Wang: Decoupling Control, Springer-Verlag, Berlin, 2003.

[13] T. Ádám, S. Dadvandipour, J. Futás: Influence of Discretization Method on the Digital Control System Performance, Acta Montanistica Slovaca, Vol 8, No. 4, 2003, pp. 197 – 200.

[14] N.J. Higham: The Scaling and Squaring Method for the Matrix Exponential Revisited, SIAM Journal on Matrix Analysis and Applications, Vol. 26, No. 4, 2005, pp. 1179 – 1193.

[15] M. Goldfarb, N. Celanovic: Modelling Piezoelectric Stack Actuators for Control of Micromanipulation, IEEE Control Systems, Vol. 17, No. 3, June 1997, pp. 69 – 79.

[16] L. Juhász, J. Maas, B. Borovac: Parameter Identification and Hysteresis Compensation of Emeded Piezoelectric Stack Actuators, Mechatronics, Vol. 21, No. 1, Feb. 2011, pp. 329 – 338.

[17] A. Granas, J. Dugundji: Fixed Point Theory, Springer-Verlag, New York, 2003.

[18] H. Harrer: Order reduction, Pflaum, Munich, 2002.

[19] L. Litz,: Reduction of the order of linear state space models using modal method, Hochshul-Verlag, Stuttgart, 1979.

[20] E. Hendricks, O. Jannerup, P.H. Sorensen: Linear Control Systems, Springer-Verlag, Berlin, 2008.

[21] S. Preitl, R.E. Precup, P.A. Clep, I.B. Ursache, J. Fodor, I. Skrjanc: Pole Placement Approaches for Linear and Fuzzy Systems, International Symposium on Intelligent Systems and Informatics, Subotica, Serbia, Sept. 2008, pp. 391 – 396.

[22] L. Juhász, A. Kiffe, J. Maas: FPGA-based Interface for Control of a Hybrid Micropositioning Stage, IEEE Industrial Electronics Society Conference, Porto, Portugal, Nov. 2009, pp. 2842 – 2847.

[23] S. Jeevananthan, R. Nandhakumar, P. Dananjayan: Inverted Sine Carrier for Fundamental Fortification in PWM Inverters and FPGA Based Implementations, Serbian Journal of Electrical Engineering, Vol. 4, No. 2, Nov. 2007, pp. 171 – 187.

[24] M. Carevic, Z. Cica: FPGA Implementation of IP Packet Segmentation and Reassembly in Internet Router, Serbian Journal of Electrical Engineering, Vol. 6, No. 3, Nov. 2009, pp. 399 – 407.